Observation of discrete concentric surface modulations on free-flying liquid tin sheets

H. K. Schubert,[1,2,a)] D. J. Engels,[1,2,a)] M. Kharbedia,[1] H. Gelderblom,[3] and O. O. Versolato[1,2,b)]
[1)]*Advanced Research Center for Nanolithography (ARCNL), Science Park 106, 1098 XG Amsterdam, The Netherlands*
[2)]*LaserLab, Department of Physics and Astronomy, Vrije Universiteit Amsterdam, De Boelelaan 1100, 1081 HZ Amsterdam, The Netherlands*
[3)]*Institute for Complex Molecular Systems and J. M. Burgers Center for Fluid Dynamics, Department of Applied Physics, Eindhoven University of Technology, Den Dolech 2, Eindhoven 5600 MB, Netherlands*

(Dated: 1 July 2025)

We report on the observation of concentric surface modulations on thin tin sheets formed from laser pulse impact on tin microdroplets (of various diameters $D_0 = 27, 31, 45, 55$, and $70\,\mu$m) at intermediate Weber (We) numbers in the range ∼1 000–7 000. By combining optical inspection in both reflection and transmission modes, we establish that the modulations, with a wavelength on the order of 15 µm, have an amplitude of the order of 10 nm on a sheet (ranging 50 to several 100 µm in radius) with an average thickness of the order of 100 nm. Surprisingly, the modulations appear to be predominantly axisymmetric. The highly reproducible modulations are interpreted as an intermediate We manifestation of the sheet modulations that cause sheet breakup for higher We numbers as investigated by Klein et al. [J. Fluid Mech. **893**, A7 (2020)]. We compare the obtained typical wavenumber and amplitude to their model, which relates the instantaneous wavenumber to the key system parameters assuming a Rayleigh-Taylor instability, although questions on the origin of the axisymmetric modulations remain.

I. INTRODUCTION

Droplet impact on solid surfaces or pillars leads to thin sheet formation[1–7]. Industrial processes that involve droplet deformation upon impact include spray coating (for example, in agriculture[8,9]), printing[10,11], and advanced EUV nanolithography systems[12,13]. Understanding the fluid dynamics of sheet formation is, therefore, critical for optimizing these applications. In state-of-the-art nanolithography machines, thin sheet formation is specifically engineered by laser-driven deformation of liquid tin droplets. An initial laser pulse, known as the pre-pulse (PP), induces an impulsive acceleration ($a \sim 10^{10}\,\mathrm{m/s^2}$) to the liquid tin droplet, initiating radial expansion of the droplet into a thin sheet target on the capillary time scale ($\sim \mu$s)[12–14]. This sheet optimizes the subsequent interaction with the main pulse, which produces plasma from the tin sheet and generates the essential extreme ultraviolet (EUV) light required for high-resolution nanolithography[15–17]. Various hydrodynamic (in)stabilities on such rapidly expanding liquid sheets, play a key role in maximizing EUV yield while minimizing liquid tin "debris"[18].

Squire conducted a foundational study on water sheet instabilities leading to atomization[19]. Taylor later confirmed the findings of Squire, demonstrating that sheet instabilities occur only when the liquid system exceeds a critical threshold[20]. Following Taylor's work, numerous studies have explored sheet instabilities using various experimental setups to better characterize and understand the underlying mechanisms. For example, Villermaux and Clanet studied sheet instabilities generated by the impact of a liquid jet on a disc[21,22], while Li et al. examined sheet instabilities arising from collisions between liquid jets[23]. Bremond and Villermaux[24] took a different approach, investigating the breakup of a thin homogeneous soap film under impulsive acceleration from a uniform shock wave, thereby inducing a Rayleigh-Taylor instability that ultimately leads to sheet fragmentation. That study revealed a time-dependent growth rate and mode selection of wavelengths λ within the range $R_0 \geq \lambda \geq \lambda_c$, where $\lambda_c = 2\pi\sqrt{\sigma/\rho a}$ represents the capillary length of the liquid system of size R_0 (the initial radius of the droplet) with density ρ and surface tension σ undergoing an acceleration a. In these studies, it has been observed that the fastest growing modes dominate the sheet surface modulation, and that the modulation amplitude is a characteristic feature of each liquid system[25,26]. Vledouts et al.[27] found that impulsive radial expansion of a dense liquid shell triggers a Rayleigh-Taylor instability, leading to destabilization of the shell and the formation of characteristic instability patterns. More recently, Klein et al.[28] investigated the fragmentation of both liquid tin and water droplets impacted by a laser pulse. They proposed that thermal noise inherently present in the laser-matter interaction seeds equally all allowed wavenumbers, assuming white noise, while the acceleration of the droplet after impact drives the selection and growth of specific modes. The fastest-growing modes eventually lead to sheet piercing when their amplitude approaches the sheet thickness. Based on these observations, scaling laws have been developed for characteristic breakup time and wavenumber, identifying specific regions of the sheet, specifically the center and edge, where modulations predominantly can be observed to influence stability[28]. These modulations have primarily been *inferred* from their impact on sheet breakup, particularly hole formation[28]. However, the behavior of instabilities on expanding sheets in the pre-breakup phase remains largely unexplored.

[a)]These authors contributed equally to this work
[b)]Author to whom correspondence should be addressed: versolato@arcnl.nl

In this work, we experimentally investigate sheet modulations arising from laser-induced deformation of tin microdroplets in a vacuum environment, in a setting similar to that of Klein et al.[28]. We employ our stroboscopic microscopy setup to capture sheet surface *reflections* along with the usual shadowgraphy images, and unveil patterns characterized by discrete concentric rings on intact sheets. These patterns appear consistently and identically on both sides of the sheet. We find that by increasing the laser pulse energy, the concentric symmetry is broken and azimuthal modulations appear to culminate in sheet breakup. The primary aim of the current study, however, is to report on the direct observation of discrete concentric modulation patterns at intermediate We numbers.

Our observations are interpreted along the lines of a model introduced by Klein et al.[28].

II. EXPERIMENTAL METHODS

Our experimental setup has previously been described in detail[29,30]. Here, we present a summary and the additions that enable the reflection measurements. A more comprehensive schematic of our measurement setup is provided in Fig. 11 in Appendix B. The experiment (see Fig. 1) employs a droplet generator to produce a kHz stream of liquid tin droplets at a temperature of 270 °C in a vacuum environment at a base pressure of 10^{-7} mbar. Droplet diameters, adjustable between 17 µm and 70 µm, travel at velocities of ∼10 m/s through a continuous-wave HeNe laser light sheet. The scattered HeNe laser light is detected through a photomultiplier tube and down sampled to 10 Hz, triggering the experiment and synchronizing all lasers at the same repetition rate.

Figure 1(a–d) illustrates the laser pulse scheme. Figure 1(a) shows the prepulse (PP), focused to a Gaussian spot with a full width at half maximum (FWHM) of approximately 100 µm at the droplet location, centered in the vacuum chamber. The PP is generated by a seeded Nd:YAG system (Continuum Surelight III, $\lambda = 1064$ nm) that emits temporally Gaussian pulses with durations ranging from $\tau = 6$ to 20 ns; the pulse length is set to 10 ns unless specified otherwise. Circularly polarized for uniform energy deposition, the PP creates plasma on the side of the droplets where it strikes, imparting an impulsive acceleration (of the order of $\sim 10^{10}$ m/s^2) that drives radial expansion into a thin sheet[14] at velocities of several 100 m/s on the time scale of the laser pulse duration. Over time, the radial expansion velocity, initially $\dot{R}_0$, decreases due to surface tension on the capillary time scale (on the order of µs), while the propulsion velocity, U, remains constant.

Figure 1(b) illustrates the vaporization pulse (VP), focused to a Gaussian spot of 1400 µm × 1280 µm at the center of the chamber. The VP, generated by a seeded Nd:YAG system (Continuum Agilite 569-12, $\lambda = 1064$ nm), emits temporally box-shaped pulses of fixed 50 ns duration. The VP is circularly polarized and vaporizes the liquid tin sheet. The vaporization rate depends on the VP intensity and typically in the experiments is of the order of a few nm/ns[30]. Under these conditions the vaporization does not lead to any appreciable acceleration.

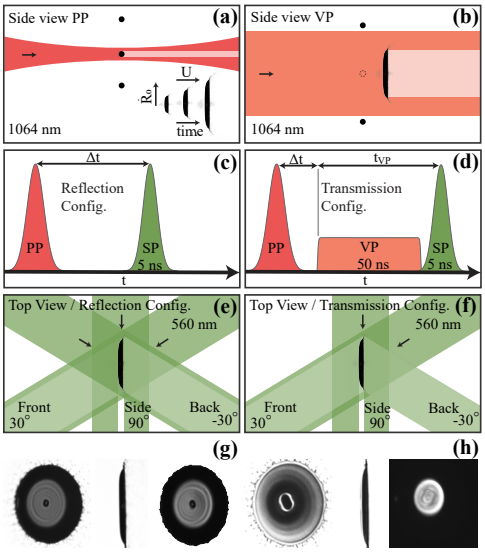

FIG. 1. (a-d) Schematic of the experiment's laser pulse schemes with irradiation geometries and timings shown. (a) Side-view schematic of the pre-pulse (PP) induced deformation dynamics. (b) Side-view schematic of the vaporization pulse (VP) irradiating the liquid tin sheet. (c) Timing of the shadowgraphy pulse (SP) relative to the PP in the reflection configuration. (d) Timing of the SP in the transmission configuration. The VP follows the PP after Δt, with the SP scanned in time over the VP. (e) Top-view schematic of the reflection configuration showing illumination geometries. (f) Top-view schematic of the transmission configuration showing illumination geometries. Shadowgraphs from front, side, and back view (31 µm, We ∼ 3 100, $\mathrm{We_d} \sim 4\,200$) (g) in the reflection configuration at $t = 0.21\,\tau_c$ and (h) in the transmission configuration slightly later at $t = 0.38\,\tau_c$.

To observe the liquid tin sheet, we use an imaging system synchronized with the PP timing [Fig. 1(c)] or VP timing [Fig. 1(d)]. In the case of Fig. 1(c), the shadowgraphy pulse (SP) is scanned (in delay steps) at a time Δt after the PP ($\Delta t = 0$ marks the center of the PP). In part of our studies we use a double-framing camera in tandem with two backlighting pulses (spaced as close as 300 ns) to enable studying dynamics on the same sheet, cf. Ref. [31]. In the case of Fig. 1(d), the SP is scanned (in delay steps) over the ongoing VP ($t_{VP} = 0$ marks the start of the VP). The VP itself impacts at a time Δt after the PP. In both cases, we use an imaging system that comprises a dye-based illumination source with 5 ns duration (FWHM), 12 nm spectral bandwidth (FWHM), 560 nm center wavelength and CCD cameras (AVT Prosilica GT2450, pixel size: 3.45 µm and PCO ultraviolet, pixel size: 4.65 µm), coupled to long-distance microscopes (K2 Distamax with CF-1/B objective). This setup provides a spatial resolution of approximately 5 µm, a numerical aperture (NA) of 0.046, and a depth

of focus of around 230 µm[32]. At each delay step, we record 20 frames in a stroboscopic manner, with each frame capturing a distinct laser-droplet interaction event. After some finite expansion time, we carefully adjusted the focus at each step for both the front and back cameras throughout the droplet deformation process.

Figure 1(e) illustrates the reflection setup. It utilizes three synchronous SPs for front, side, and back view imaging at angles of 30°, 90°, and 150° relative to the laser axis, respectively, and enables observing reflection patterns from both sides of the sheet along the droplet deformation process. Figure 1(f) presents the transmission setup, which utilizes two synchronous SPs for front and side imaging at angles of 30° and 90°, respectively, relative to the laser axis. This setup enables the observation of liquid tin sheet dynamics during VP irradiation and has been previously employed to study the vaporization mechanism in detail[30]. Those previous studies[30] have shown that irradiating liquid tin sheets with VP at intensities below $5\times10^7\,\mathrm{W/cm^2}$ induces Hertz-Knudsen evaporation, gradually reducing the sheet thickness at a constant, intensity-dependent rate. As a result, the SP transmission through the sheet increases with each successive delay step. We extract the raw optical transmission values pixel by pixel, applying corrections for backlight intensity fluctuations, additional glare sources, and the 30° observation angle. Using the TMM[33] Python package, we establish a relationship between these corrected transmission values and the sheet thickness. In summary, this process integrates an established method to correlate SP transmission values through the liquid tin sheet with its corresponding thickness[30,31].

III. RESULTS

Figure 1(g) presents example shadowgraphs obtained with the reflection setup, showing front, side, and back views (left to right). The front view captures the sheet illuminated from the back side, with reflections from the front illumination visible on the inner part of the sheet. Next, the side view reveals a non-trivial curvature of the sheet: the sheet is not flat but at its edges curves away from the laser. Finally, the back view shows the sheet illuminated from the front, with reflections from the back illumination visible on the inner part of the sheet. Note that we employed image-processing techniques to enhance the visibility of the inner reflecting area in the back view while maintaining a consistent background across all shadowgraphs acquired with the reflection setup for this example. This adjustment accounts for the varying background illumination intensities between the front and back views. The acquisition reveals that only an inner region of the sheet reflects light, as the sheet's curvature causes the relatively large surface angles outside this region to reflect incoming rays outside the NA of the imaging system (see below). More importantly, the reflection of the inner part of the sheet is not uniform but displays a discrete concentric pattern. This reflection pattern suggests the presence of a discrete concentric modulated sheet profile that appears to be similar on both sides.

Figure 1(h) shows example shadowgraphs obtained with the transmission setup from front, side, and back views (left to right). In this setup, the front view captures the sheet under back illumination during the vaporization pulse. The shadowgraphs clearly show the presence of the main features of the target: center mass, sheet, bounding rim, ligaments, and fragments[31]. We observe gradual mass removal from the sheet with increasing t_{VP} through the increase in transparency of the sheet to shadowgraphy backlight illumination in line with prior works (e.g., see[30]). The front view highlights the presence of discrete concentric regions with greater thickness, indicating a *thickness* modulation of the sheet profile as vaporization occurs at a globally constant, intensity-dependent rate[30]. The side view shows another perspective of the vaporization progress, while the back view captures back illumination reflections from the inner, thicker, yet not-yet-vaporized part of the sheet.

In our experiments, the PP laser energy can be adjusted, directly influencing two key parameters: the propulsion Weber number (We) and the deformation Weber number ($\mathrm{We_d}$) following e.g. Refs. [28,31]. These two parameters are defined as follows:

$$\mathrm{We}=\frac{\rho U^2 D_0}{\sigma},\quad \mathrm{We_d}=\frac{\rho \dot{R}_0^2 D_0}{\sigma}. \tag{1}$$

Here, $\rho=7000\,\mathrm{kg/m^3}$ and $\sigma=0.55\,\mathrm{N/m}$ represent the density and surface tension of the liquid tin, respectively, while D_0 is the initial droplet diameter[34,35]. We extract the propulsion velocity (U) and initial expansion velocity ($\dot{R}_0$) from shadowgraph images [cf. Fig. 1(g)], with U measured from side-view images (1âĂŞ4 µs) and $\dot{R}_0$ from front-view images (200âĂŞ500 ns). As we will explain below (see Sec. IV), the propulsion Weber number (We) seeds and mode-selects a Rayleigh-Taylor-type instability[28], while the deformation Weber number ($\mathrm{We_d}$) drives sheet expansion[35] and with it the stretching of the surface modulations (along with the other dynamics relevant for target preparation[18]). The ratio of the two Weber numbers $\mathrm{We_d/We}$ is of order unity and typically reduces with laser pulse energy and length[36]. The droplet deforms into a sheet-type target on an inertial time scale $\tau_{\mathrm{i}}=D_0/U$ and the overall sheet expansion process occurs on a capillary time scale $\tau_{\mathrm{c}}=\sqrt{\rho D_0^3/6\sigma}$. We note that the definitions of We, $\mathrm{We_d}$, and τ_{c} used here differ from those in Klein et al.[28] to adhere to a more consistent notation by using D_0 in all combined equations.

In the following, we first discuss in detail the observations obtained using the reflection setup (Sec. III A), followed by those obtained using the transmission setup (Sec. III B). For an overview of the parameters used, refer to Tab. I in the Appendix.

A. Reflection

By varying the laser pulse energy, and with it the Weber number, we observe changes in the reflection patterns. Figure 2(a-d) presents shadowgraphy images of expanding sheets at time $t=0.2\tau_{\mathrm{c}}$ of a 31 µm droplet for increasing We. At

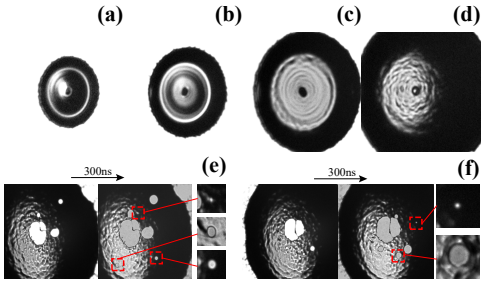

FIG. 2. Front view reflection shadowgraphs of 31 µm-diameter droplets subjected to a 10 ns laser pulse at a common non-dimensionalized time $t = 0.2\tau_c$ for: (a) We = 800, We_d = 1 200; (b) We = 1 700, We_d = 2 300; (c) We = 4 700, We_d = 5 800; and (d) We = 12 000, We_d = 10 600. The lower row (e, f) shows (at $t = 0.3\,\tau_c$) 50 µm-diameter droplets exposed to a 15 ns laser pulse, achieving approximately We = 123 000, We_d = 57 000. For both cases, the left image depicts the initial state, while the right image shows the *same* sheet 300 ns later using a double-framing camera (see the main text).

(for the current work) relatively low We numbers we observe discrete concentric reflection patterns. At higher We, the concentric reflection pattern develops azimuthal components, i.e., angular modulations around the sheet's center that perturb the predominantly concentric rings. We observe that azimuthal modulations begin at the outer radii earlier than at the inner radii, indicating perhaps an additional dependence on sheet thickness and time, driven by continuous thinning during droplet deformation[31] or sheet radius. We find that the azimuthal modulation wavelength is of similar order as the wavelength of the concentric modulation. At even higher We the pattern randomizes with no clear symmetry. This observation indicates a transition from discrete concentric to azimuthal modulations with randomized phases, similar in appearance to the work of Xia et al.[37].

For the highest We numbers, hole formation becomes evident in line with Refs. [28,31], with the amplitude of the perturbations reaching a magnitude similar to the local thickness of the liquid sheet[28]. To better understand both the reflection pattern and hole formation, we present shadowgraph images in Fig. 2(e, f) showing two example sheet breakup events of a 50 µm-diameter droplet at $t = 0.3\,\tau_c$ with a very high We of approximately 123 000, using a double-framing camera in tandem with two backlighting pulses, to enable capturing the dynamics of specific single holes. Each panel shows the initial sheet state (left) and the same sheet just 300 ns later (right). The initial shadowgraphs reveal preexisting holes in the liquid tin sheet, while the subsequent frame captures newly formed holes (marked with red circles) and their growth following Taylor-Culick[28,31]. These shadowgraphs demonstrate that our setup enables direct observation of sheet modulations in reflection prior to sheet breakup.

As holes open, they induce additional radial modulations (lower inset in Fig. 2(f)) and lead to ligament formation, as reported by Vledouts et al. [27]. Importantly, the connecting ligament between the center mass and the sheet provides clear evidence that the center mass remains physically connected to the sheet prior to hole formation. While hole formation highlights later stages of sheet evolution, the earlier stages of surface modulations also offer valuable insights. At intermediate We values around 2 300, as shown in Fig. 2(b), the sheet exhibits a striking discrete concentric reflection pattern. This pattern facilitates clearer analysis, including comparisons between front- and back-view acquisitions, allowing a more detailed understanding of the instability's growth rate and propagation.

In summary, Fig. 2 shows that the laser-on-droplet impact causes various types of reflection patterns depending on the Weber number. We hypothesize that these reflection patterns share a common underlying primary instability mechanism, similar to the Rayleigh-Taylor type proposed by Klein et al.[28] (see discussion in Sec. IV below). At lower We, we observe discrete concentric reflection patterns that are more easily traceable; these will be the main focus of the current study.

We next qualitatively examine the temporal evolution of the reflection pattern for a low We. Figure 3 illustrates the sheet expansion of a 31 µm droplet with a low We of $\sim$ 1 700 shown from the (a) front, (b) side, (c) back and (d) combined front/back views. For each delay step we average 20 frames to improve the signal-to-noise ratio. During the characteristic sheet expansion following impact (see Ref. [5]), an inner region on both sides of the sheet reflects the green shadowgraphy light. The radial extent of this reflective region roughly follows the overall trajectory of the expanding sheet. This contraction arises from the temporal evolution of the global sheet curvature. As the curvature evolves, the sheet's surface angles increasingly reflect light outside the NA of the imaging system, causing those regions to be dark. Consequently, the reflective region is limited to those areas where the sheet's surface angles allow reflections within the NA, as we will explore in more detail in Sec. III A.

Figure 3(d) highlights that during the sheet expansion, the inner reflective region exhibits discrete concentric reflection patterns that are highly similar (within a fraction of the wavelength) in both the front (left) and back (right) views, suggesting a coupling between the concentric modulated surfaces of the sheet. Noticeable differences between the front and back views are primarily observed near the center mass.

We identify an onset time of discrete concentric reflections on both sides around $t = 0.19\,\tau_c$. At this time, the thickness of the inner reflective region is estimated to be larger than $\sim$500 nm, based on a thickness model for liquid tin sheets provided by Liu et al. [31]. This suggests that the surface modulations are coupled already in the early stages of the droplet deformation. At earlier times, such as at $t = 0.13\,\tau_c$, the back curvature differs from the front curvature, as no concentric reflection patterns are observed in the back view in line with a Rayleigh-Taylor scenario (see below) in which the laser-facing surface destabilizes first. Although discrete concentric reflections may still form earlier during the expansion, we do

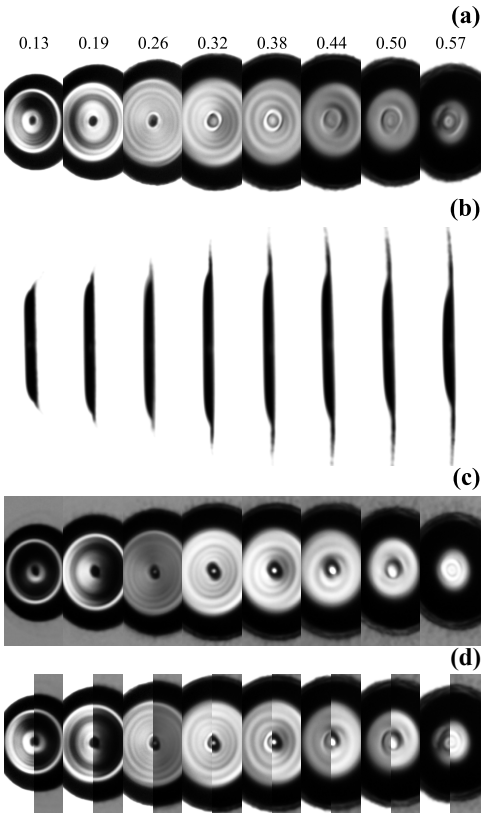

FIG. 3. Shadowgraphy images of sheet expansion of a 31 µm diameter droplet, propelled to We = 1 700, and We_d = 2 300 in (a) front view, (b) side view, (c) back view, and (d) combined front view (left) and back view (right) comparison. Numbers on the top indicate the non-dimensional time t/τ_c.

not detect them perhaps due to limitations in resolution and in the focusing of the imaging systems throughout the expansion.

As the sheet expands, the surface modulations responsible for the reflections stretch over time, with a closer spacing observed at earlier times (e.g., compare $t/\tau_c = 0.26$ with $t/\tau_c = 0.44$).

Also, the data hint at a wavelength that is a function of the radial coordinate, with larger spacings between bright rings towards the large radii (cf. Fig. 3(a) near $t/\tau_c = 0.26$). Around the sheet expansion apex ($t/\tau_c = 0.38$), we may extract a typical modulation wavelength of approximately 15 µm as the difference between two bright rings.

In the following, we address several open questions. What sheet morphology causes the observed discrete concentric reflections? What are typical amplitudes of these surface modulations? Finally, can we argue that these surface modulations are symmetrically phased?

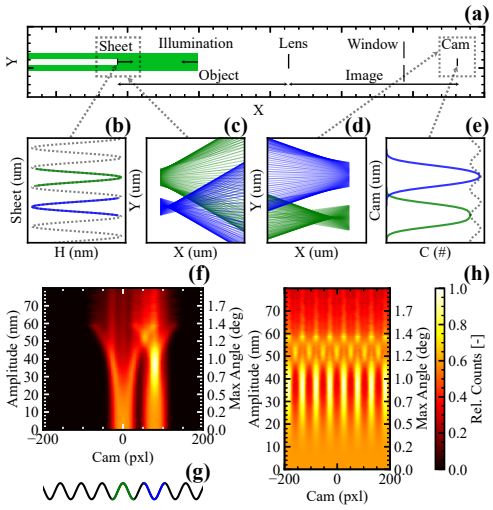

FIG. 4. (a) Overview of the ray tracer model, showing key components: illumination source, sheet, window (1.5"), lens (2"), and camera chip. (b) Close-up of a model sheet with a sinusoidal modulation of 15 µm wavelength and 15 nm amplitude, highlighting a single hill (green) and a sink (blue). (c) Reflected rays near sheet hill and sink. (d) Ray convergence on the camera chip. (e) Ray count on the camera chip corresponding to sheet hill and sink, with total ray count (grey). (f) Ray distribution on the camera chip as a function of amplitude for isolated sheet features highlighted in (g). (h) Ray distribution for the full sinusoidal surface.

To interpret the reflection measurements, we utilize an in-house developed 1-D raytracer to correlate the reflection intensity recorded on the camera chip with height modulations on the sheet surface. Fig. 4(a) depicts the modeled setup in side view with the illumination and camera positioned in the same plane for simplicity (i.e., back illumination and back camera). It illustrates the raytracer model setup and its key components, while Figs. 4(b, c, d) provide zoomed-in views of an example simulation. In the simulation, a spatially box shaped illumination pulse is used and the lens is modeled as ideal, with a constant focal length across its surface. Rays are initialized from the light source and directed toward the sheet, which is assigned a sinusoidal modulation with adjustable parameters such as amplitude (η) and wavelength (λ) at any radial location on the sheet (r) in $y = \eta\cos(2\pi/\lambda r)$. A sinusoidal modulation with a wavelength of 15 µm is chosen, in line with the typical wavelength that may be observed in the experiment cf. Fig. 3. Figure 4(b) depicts an example sinusoidal modulation, highlighting a hill (green) and sink (blue) regions. Upon reaching the sheet, rays are reflected specularly. As shown in Fig. 4(c), hill regions cause ray divergence,

while sink regions lead to focusing. Reflected rays then propagate further and encounter the lens, where they are refracted according to Snell's law. Figure 4(d) shows the rays after lens refraction, just before reaching the camera chip that is placed in the image plane. Due to the single-lens imaging system, the reflected image is inherently flipped. A zoomed-in view near the camera chip highlights how blue rays (from sinks) accumulate on the chip, creating bright regions, while green rays (from hills) diverge, resulting in dimmer regions. Finally, Fig. 4(e) presents the accumulated counts within each camera pixel (3.45 µm), with the gray line indicating the total counts if the full sheet reflects. This example simulation shows that a hill (green) causes lower count on the camera chip than a hill (blue).

We demonstrate that our raytracer simulation effectively maps reflection points on the sheet to their corresponding positions on the camera sensor. The simulation reveals that the bright, discrete concentric reflections observed on the sensor originate from surface sinks.

Building on this insight, we investigate the effect of varying sheet modulation amplitudes. Note that in the following, the sheet and counts are plotted from the perspective of the camera. Figure 4(f) presents a heatmap of the camera count distribution as a function of sheet modulation amplitude for selected regions of a sinusoidal modulated sheet profile. These regions are highlighted in Fig. 4(g), with a hill marked in green and a sink marked in blue.

At very low amplitudes, both hill and sink produce similar count patterns, as the amplitude increases, the hill count pattern spreads a bit and loses contrast, while the sink pattern shows an increase in contrast, maximizing between 30–40 nm. At higher amplitudes, some interference occurs between the reflecting regions on the sheet, and beyond 60 nm, the camera counts diminish because of the NA limit. The right axis of the heatmap indicates that the maximum observable surface angle is approximately 1.42° (corresponding to a full surface angle of $\theta = 2.84°$ and NA of 0.049). This aligns with our experimental setup and supports the conclusion regarding why only an inner region reflects, as shown in Fig. 3. Beyond this maximum angle, imaging of the SP reflection becomes impossible due to the NA limitations of the experimental setup. The local sheet surface normal can exceed this angle, for instance, in cases of large modulation amplitudes or high curvature, and would then produce a dark region.

Figure 4(h) presents a heatmap of camera counts for a fully reflecting sinusoidally modulated sheet profile, illustrating both the maximum observable surface angle and the interference patterns that again arise at higher amplitudes. We note that both heatmaps [Fig. 4(f,h)] are globally normalized, making it difficult to identify differences between hills and sinks at low amplitudes. At around 10 nm amplitude, these contrast differences (ratio of count values between maxima and minima) are approximately 4 %; at 30 nm amplitude the contrast already increases to approximately 50 %.

Next, combining raytracer insights (Sec. III A, Fig. 4) with experimental shadowgraphs (Sec. III A, Fig. 3), we arrive at the following conclusions. We learn that dark regions in shadowgraphs correspond to reflections from surface modulations (hills). The phase-relation question is resolved: a hill decreases the camera count, while a sink increases it. From the reflection measurements, it is observed that the surface reflections are approximately in a fixed phase, meaning a bright spot in the front view corresponds to a bright spot in the back view. This suggests a symmetric relation between the sheet surfaces, with both surface modulations being out-of-phase (i.e. they are mirror symmetric, see schematic in Fig. 5). The contrast that is typically observed for good ripple observation cases in the experiments [such as those shown in Fig. 3(a)] lies at the level of 5–10%, which, following the simulations, would be consistent with a modulation amplitude of approximately 10–15 nm in this specific example. Assuming a symmetric sheet instability, the thickness variation indicates that the thickest regions are given by $h_m = h_0 + 4\eta_0$. Of course, any nonzero phase (Φ) would reduce the thickness, as is illustrated in Fig. 5.

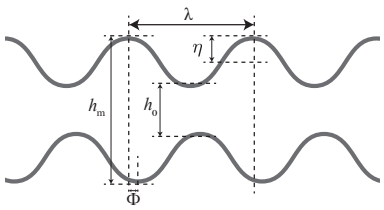

FIG. 5. Schematic of a symmetric sheet instability with modulation amplitude η, modulation wavelength λ undisturbed sheet thickness h_0, disturbed thickness h_m, and phase Φ.

B. Vaporization

We apply a vaporization pulse [see methodology in Fig. 1(b, d, f, h)] to a liquid tin sheet to better understand its modulation by studying variations in thickness as enabled by the vaporization method, following Ref. [30]. Specifically, we aim to validate the relative amplitude of the modulation (η) under the assumption of a symmetric sheet instability (see Fig. 5). First, we link the reflection and transmission data and then estimate the thickness of the observed modulations.

In Fig. 6, we generate an intermediate We = 3 100 with concentric modulations and compare shadowgraphs recorded using the reflection and transmission setups. This slightly higher We compared to Fig. 3 is chosen to improve comparability between the reflection and transmission setup. We trade off visibility of the reflections (best seen at low We) for transmission (best at high We numbers where sheets are thin).

Figure 6 shows shadowgraphs from the reflection setup (left) and the transmission setup (right) at (a) $t/t_c = 0.24$ and (b) $t/t_c = 0.38$. The reflection shadowgraph has been discussed in detail in Sec. III A. The transmission shadowgraph is obtained by applying a VP, which induces gradual thinning of the sheets thickness profile[30] [also see the schematic in Fig. 1(f)]. For this We value, the thinning process results

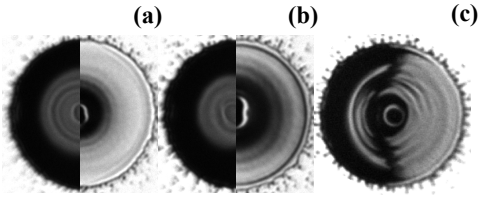

FIG. 6. Front view reflection shadowgraph (left) alongside a front view transmission shadowgraph (right) of the same We but a different frame [31 µm droplet diameter, We $\sim$ 3 100, $\mathrm{We_d} \sim$ 4 200] at (a) $t/\tau_c = 0.24$ and (b) $t/\tau_c = 0.38$. (c) A liquid tin sheet irradiated only locally by a modified VP, leading to predominant vaporization on the right side while reflecting SP light on the left side [36 µm diameter droplet, $t/\tau_c = 0.31$, We $\sim$ 1 400, $\mathrm{We_d} \sim$ 3 900]. In both panels, the shadowgraphs have been adjusted (they are horizontally stretched) to account for the observational angle of 30°.

in the formation of dark concentric rings. These rings correspond to regions of greater sheet thickness, as the evaporation is governed by a globally constant, intensity-dependent rate that is independent of the instantaneous thickness[30].

More specifically, in Fig. 6(a), right-hand side, we select a transmission shadowgraph captured along a VP irradiation delay scan, where free-flying thickness modulations are clearly visible. Both reflection and transmission measurements exhibit patterns with closely matching periodicity, confirming the presence of surface modulations and that their mutual phasing leads to thickness variations in the liquid tin sheet's profile.

The transmission shadowgraph also highlights that, due to the sheets thickness gradient[31], the outer parts of the sheet evaporate earlier than the inner parts. As a result, thickness modulations in the sheet thickness profile at the outer radii become visible and fully vaporize earlier than those closer to the center.

With continued VP irradiation, the inner parts of the sheet begin to exhibit finite transmission, leading to the unraveling of the inner sheet thickness modulations, while fully vaporizing the outer ones. This dynamic not only confirms the presence of thickness modulations but also provides a basis for quantifying their thickness (see below).

To compare reflection and transmission over a larger sheet area, we acquire shadowgraphs later in the droplet deformation process at $t/\tau_c = 0.38$, as shown in Fig. 6(b) for the same We. At this stage, the reflection pattern shows noticeable changes, with the inner reflective area being slightly reduced in size compared to earlier times. This observation is consistent with that for the slightly lower We case shown in Fig. 3. The time $t/\tau_c = 0.38$ corresponds to the sheet expansion apex, where the thickness gradient is much weaker, resulting in a more homogeneous thickness profile[31] which benefits visibility of any thickness modulations over a large area. This example demonstrates that a low thickness gradient does not necessarily correlate with the curvature of the sheet. At this time, the thinner sheet exhibits a smaller area reflecting into the NA of the imaging system (cf. Sec. III A).

In contrast, the transmission measurements reveal thickness modulations in the sheet that are not observable in reflection. This confirms that these thickness modulations persist throughout the droplet deformation process and emphasizes that each methodology has a distinct observational window: For the reflection setup, optimal conditions require a locally flat sheet, whereas for transmission, a more homogeneous sheet thickness profile is preferred instead. In this sense, the reflection and transmission methods give a complementary view of the surface modulations.

Finally, we compare reflection and transmission shadowgraphs by optimizing the conditions for both setups for the same sheet. This is achieved by selecting We = 1 400 and $t/\tau_c = 0.31$, as shown in Fig. 6(c). We vaporize only the right side of the sheet using a VP intensity that induces evaporation up to the sheet center. Even in this case, despite the high similarity and consistent wavelength of patterns observed in reflection and transmission, we cannot draw definitive conclusions about the exact relationship between the bright (or dark) concentric reflections in the reflection shadowgraph and the dark concentric rings in transmission, because of poor contrast in the transition area.

In the following, we use the VP to estimate the sheet thickness and, from the thickness, derive the amplitude of the modulation assuming a symmetric sheet instability (see Fig. 5).

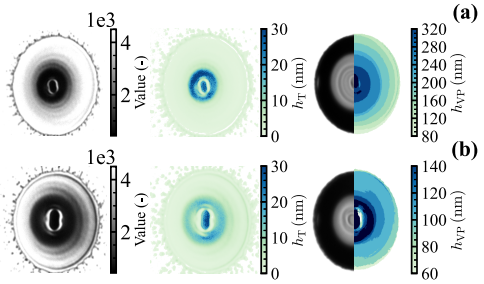

FIG. 7. Shadowgraph images and analysis. From left to right: partially vaporized sheet, corresponding thickness map using transmissivity method (see Ref. [30]) and reconstructed sheet thickness map by using the vaporization time and vaporization rate. Both rows show data for a 31 µm diameter droplet propelled to We $\sim$ 3 100 and $\mathrm{We_d} \sim$ 4 200 at time (a) $t/\tau_c = 0.24$ and (b) $t/\tau_c = 0.37$.

Figure 7 shows liquid tin sheets in the leftmost column at two different times during the droplet deformation process: (a) at $t/\tau_c = 0.28$ and (b) at $t/\tau_c = 0.37$. At both expansion times, a VP delay scan is performed. The left column shows a frame of the VP delay scan that highlights the progress of vaporization and the presence of thickness modulations. For both VP delay scans, the VP intensity is carefully adjusted to achieve sufficient vaporization of the sheet at the end of VP irradiation, resulting in evaporation rates[30] of 6.4 nm/ns and 2.6 nm/ns, respectively, as explained in more detail below.

The middle column of Fig. 7 shows direct thickness maps

(h_T), obtained from the transmission shadowgraphs in the leftmost column using the transmissivity method (for further details, see Sec. II). In both cases, concentric thickness modulations are evident, but are challenging to resolve directly in thickness.

The right column shows the reconstructed sheet thickness profile (h_{VP}). The sheet profiles are obtained as follows: First, we align all shadowgraphy frames for each delay step (t_{SP}) during VP irradiation. Next, we determine pixel-wise vaporization times by evaluating whether a pixel has been vaporized in more than 50 % of the frames for a given delay. We then calculate the sheet thickness maps by multiplying the pixel-wise determined delay values t_{SP} with the vaporization rate $\dot{h}$, such that $h_{VP} = t_{SP} \times \dot{h}$. We define a pixel as vaporized if its value reaches 30 % of the green SP backlight illumination through the sheet at a refractive index of $n = 1.7 + 5.1\,j$ (corresponding to 1100 K, see Ref. [38]), indicating a residual sheet thickness of 6 nm as calculated using the TMM[33] Python package. The thickness threshold is set to 6 nm because the sheets were not fully vaporized at the end of the VP irradiation. Thus, regions with thicknesses exceeding 6 nm at the end of the VP irradiation are represented as dark blue areas in the reconstructed thickness maps, indicating unknown thickness. Note that we thereby underestimate the thickness in these areas; however, this is of no substantial consequence as we focus on differences in thickness, as explained below. We determine the value of $\dot{h}$ by fitting the sheet thickness values to the profile calculated with the thickness model for liquid tin sheets as introduced by Liu et al. [31]. Additionally, we correct the obtained thickness for the observational angle of 30°.

The rightmost heatmap may suggest a stepwise reduction of the sheet radius. However as shown in[30], evaporation occurs gradually. The apparent stepwise reduction is instead caused by the shadowgraphy scan step size of $\Delta 5$ ns, which results in a delay step-wise thickness reduction given by $h = \Delta t_{SP} \times \dot{h}$. In case (a), the step-wise reduction is approximately 30 nm, while in case (b), it is approximately 13 nm. Since we compare the reconstructed thickness map with the transmission shadowgraph, we can infer that a height modulation is on the order of a vaporization step, providing an upper limit for the thickness modulation. As the sheet shown in row (a) is measured earlier in the expansion curve than (b), the sheet is thicker[18], and the VP intensity required to sufficiently vaporize it by the end of the VP duration is higher, resulting in (intentional) differences in the vaporization rate. The observation that the thickness modulation is of the order of one vaporization step then tentatively hints that the sheet in row (a) has thicker modulations than the one in row (b). This, in turn, may suggest that the thickness modulations decrease over time, which we hypothesize occurs due to a radial and temporal-dependent stretching (see Sec. III A). Furthermore, a radially dependent stretching would imply that the thickness modulations at radii farther from the center are thinner than those closer to the center. As we previously outlined, the reflection and transmission setups provide complementary measurements (see Fig. 6). Here, a full vaporization of thickness modulation primarily occurs at larger radii where reflections are not observed, potentially probing thinner thickness modulations. Thus, this approach offers an upper estimate for the thickness modulation within the vaporized radii.

We now interpret the observed thicknesses in the context of the predicted symmetric sheet instability, inferred from the reflection patterns that are highly similar in back and front view, combined with raytracer insights, which suggest that only identical sheet features can produce the observed reflection patterns. In the case of a perfectly symmetric mode, the thickest part of the sheet would be $h_m = h_0 + 4\eta$ (see Fig. 5). For the estimated modulation thicknesses, the corresponding derived amplitudes are approximately in the range of $3-8$ nm. In a direct comparison between simulation and reflection pattern at $t/\tau_c = 0.28$, we achieve contrast ratios similar to the experimental using a raytracer amplitude of about 12 nm cf. Fig. 4(h). These complementary estimates of the amplitudes are reasonably consistent given (i) the uncertainty in the VP method (and limited step size); (ii) the fact that the reflection amplitude may only be obtained from the inner part of the sheet and the thickness from the outer part. It may well be that, indeed, modulation amplitudes reduce with the radial coordinate. Additionally, it is possible that the two surfaces of the sheet are not perfectly symmetrically coupled in this specific measurement: any phase shift Φ of the surface modulation would result in a reduced overall thickness and, consequently, a smaller inferred amplitude (see the schematic in Fig. 5).

We next aim to understand how the location of the peak of the plasma pressure influences the symmetry and distribution of the modulations. By adjusting the timing of the arrival of the PP, we can adjust the laser-to-droplet alignment[39]. Such alignment adjustments lead to a tilt of the sheet, as shown in side view in Fig. 8(a). For consistency, the PP energy is tuned for each (intentional) misalignment condition such that the propulsion velocity remains approximately constant. To enable clear observations of thickness modulations after vaporization, we set PP energies (and, thus, We numbers) to values such that some azimuthal modulations occur, but concentric ripple patterns still remain dominant. Measuring the reflection pattern is not feasible in this case, as the tilt creates curvature with a surface normal that reflect light outside the NA of the imaging system. We observe that a negative misalignment (that is, the laser strikes the towards the upper pole of the droplet) leads to a negative tilt angle (cf. the -21.0° example in Fig. 8). This negative misalignment leads to a much more rapid expansion of the top part of the sheet, given there is less mass to be accelerated, and makes that the center mass appears in the bottom half of the sheet. We observe that the thickness modulations are not simply concentric around the sheet center but instead are centered around its shifted center mass. Thus, we conclude that the concentric pattern is centered at the location of the peak pressure.

IV. DISCUSSION

We next interpret our observations with the instability model proposed by Klein et al. [28], which provides estimates for the characteristic breakup time t_s and wavenumber k_s

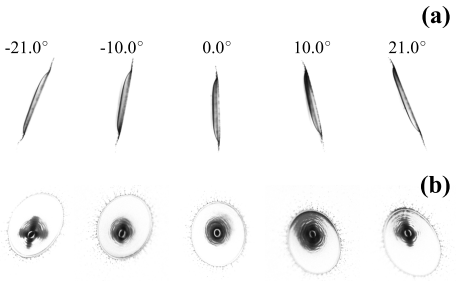

FIG. 8. Side (a) and front view (b) shadowgraphs from partially vaporized targets for different PP misalignment conditions (resulting tilt angles are shown), for a 27 µm diameter droplet hit by a PP propelling to We ≈ 7000, observed at a time $t/\tau_c \approx 0.4$.

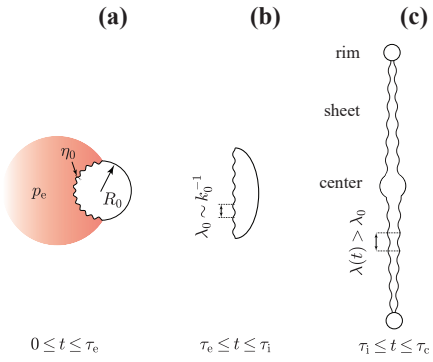

FIG. 9. Schematic based on the Rayleigh-Taylor instability-type model proposed by Klein et al.[28], illustrating three distinct phases: (a) acceleration, (b) expansion, and (c) stretching, each associated with their respective time scales. The symbols used are η_0 (initial amplitude), p_e (plasma pressure), R_0 (initial droplet radius), and τ_e (acceleration time); λ_0 (initial wavelength), k_0 (initial wavenumber), τ_i (inertial time scale); $\lambda(t)$ (wavelength over time); and τ_c (capillary time).

for highly modulated sheets. They suggest that a Rayleigh-Taylor (R-T) type instability may be triggered on the laser pulse "ejection time scale" τ_e[28], during which the liquid tin droplet experiences an acceleration $\sim U/\tau_e$. This acceleration is caused by pressure exerted by the laser-induced plasma normal to the surface of the still spherical droplet, leading to the amplification of any perturbations present on the interface of the droplet. The amplified perturbations continue to evolve inertially in the absence of an external acceleration (which ends with the laser pulse), and are affected by capillary forces on a dynamically changing topology of the evolving sheet. The model describes the evolution of the instability during the droplet deformation process. Here we interpret our findings along the same lines. In the following, we use the non-dimensional expressions for wavenumber $\hat{k}$ and time $\hat{t}$:

$$\hat{k} = kR_0, \qquad \hat{t} = \frac{t}{\tau_c} \tag{2}$$

with R_0 as initial droplet radius. The model defines three phases (see Fig. 9), in brief:

1. **Acceleration Phase** $(0 \le t \le \tau_e)$:

   During this phase, the droplet undergoes an impulsive acceleration driven by the laser-induced plasma over the (very short) duration of the laser pulse (τ_e). The plasma introduces thermal (white) noise, which seeds permissible wavenumbers $1 \le \hat{k} \le \hat{k}_c$ on the liquid, with $\hat{k}_c = \sqrt{\rho a R_0^2/\sigma} = \mathrm{We}^{1/4}\tau_e^{-1/2}$ the capillary wavenumber[28]. The acceleration sets a growth rate for the permissible R-T unstable modes with an initial amplitude η_0 and associated wavenumber k. At the end of phase 1 each mode has a specific growth rate while the corresponding normalized amplitude is still equal to unity given that the modes did not yet have any time to grow, given the impulsive nature of the acceleration.

2. **Expansion Phase** $(\tau_e \le t \le \tau_i)$:

   Following the acceleration, the droplet transitions into a flattened, sheet-like structure. In the absence of acceleration, the excited modes inherited from phase 1 continue to evolve inertially due to the velocity (growth rate) they acquired during phase 1 (see Ref. [28] for the detailed derivation). The fastest-growing mode at the end of phase 2 is given by:

   $$\hat{k}_{\max} = \frac{\mathrm{We}^{1/4}}{\sqrt{3\hat{\tau}_i}}, \tag{3}$$

   with phase 2 ending at $\hat{\tau}_i = \mathrm{We}_d^{-1/2}$. This enables rewriting Eq. (3) to obtain:

   $$\hat{k}_{\max} = \sqrt{\mathrm{We}_d}\frac{1}{\sqrt{3}}\left(\frac{E_{k,cm}}{E_{k,d}}\right)^{1/4}, \tag{4}$$

   where we introduced an energy partitioning ratio[28] $E_{k,d}/E_{k,cm} = \mathrm{We}_d/\mathrm{We}$ (the equivalence here would require a different, but constant prefactor to be absorbed in the We_d definition, following Ref. 28 contrasting Ref. 18) to translate between the two We numbers and the underlying kinetic energy in deformation vs translation. Given that both We numbers (We, We_d) play a role in the three-phase model, the introduction of the energy partitioning allows the final result (see below) to be expressed using only We.

3. **Stretching Phase** $(\tau_i \le t \le t_s)$:

   We enter phase 3 when the droplet has truly deformed into a thin sheet, with $R/R_0 \gg 1$, accompanied by a significant thinning. The model assumes that the two

opposing surfaces interact and couple, as their spacing satisfies the condition $\hat{h}\hat{k} \sim 1$[28].

For $t > \hat{\tau}_\mathrm{i}$, the wavenumber evolution is:

$$\hat{k}(\hat{t}) = \frac{\hat{k}_\mathrm{max}}{\hat{R}(\hat{t})}. \tag{5}$$

The dynamics of the sheet expansion $\hat{R}(\hat{t})$ is well understood, and can at early times $\hat{t} \ll 1$ be approximated as[28]

$$\hat{R}(\hat{t}) = \sqrt{3\mathrm{We}_\mathrm{d}} \cdot \hat{t}, \tag{6}$$

which with unity prefactor (following Ref. [28]) leads to:

$$k(\hat{t}) = \frac{(E_\mathrm{k,cm}/E_\mathrm{k,d})^{1/4}}{3\hat{t}R_0}. \tag{7}$$

The corresponding amplitude of the modulations $\hat{\eta} = \eta/R_0$ follows from[28]

$$\hat{\eta}(\hat{t}) = \hat{\eta}_0 \hat{h}(\hat{t}) \mathrm{We} \left(\frac{E_{k,d}}{E_{k,cm}} \right)^{1/4} \hat{t}, \tag{8}$$

where $\hat{h} = 4/3\,(R_0/R)^2$ is the average sheet thickness, and $\hat{\eta}_0$ is the initial perturbation amplitude. For this initial noise we find $\hat{\eta}_0 = 1.3 \times 10^{-2}$ as determined by Klein et al.[28] from experiments, assuming that the sheet punctures at a time $\hat{t}_b$ when $\hat{\eta}(\hat{t}_b) = \hat{h}(\hat{t}_b)$, with $\hat{h}$ determined from the average thickness ansatz. However, work by Liu et al.[31] has shown that the actual sheet thickness is significantly lower ($2-5\times$ depending on We and $\hat{t}$) than the average thickness, which proportionally reduces the initial noise value obtained by Klein et al.[28]. Consequently in the following we use a range $\hat{\eta}_0 = 3 - 7 \times 10^{-3}$.

From Eq. (7) we observe that the modulation wavelength is primarily a function of the non-dimensional time inversely proportional to the droplet radius and independent of the We number. We note that the energy partitioning ratio $E_\mathrm{k,cm}/E_\mathrm{k,d}$ weakly varies with laser pulse energy[28] (also see Ref. [36]). In the current analysis we may assume $(E_\mathrm{k,d}/E_\mathrm{k,cm})^{1/4} \approx 1$[28]. At the apex of the sheet expansion trajectory, $\hat{t} \approx 0.38$[18] we obtain a typical approximate modulation wavenumber $k \approx 1/R_0$. For the key data shown in Fig. 3 for a 31 µm diameter droplet, we obtain a predicted wavelength $\lambda \approx 110\,\mu\mathrm{m}$, a number that should in order of magnitude be compared to the several 10 µm in the experiments [e.g., we extracted 15 µm from Fig. 3(a)]. The corresponding amplitude of the modulations follows from Eq. (8), which gives $\eta \approx 40 - 90\,\mathrm{nm}$. This number should be compared to the order ∼10 nm amplitude we obtain from the experiments. Of course, the relation Eq. (6) is a simplified description of the instantaneous sheet radius and instead we know that $\hat{R}(\hat{t}) = \sqrt{\mathrm{We}_\mathrm{d}}\mathrm{P}(\hat{t})$ with known[18] polynomial $\mathrm{P}(\hat{t})$ which yields $\mathrm{P}(0.38) = 0.14$ and brings down the prediction to a closer match to the experiments with $\lambda \approx 42\,\mu\mathrm{m}$. However, the validity of using the instantaneous sheet radius to describe the stretching instead of Eq. (6) is an open question.

Finally, we qualitatively test the validity of the scaling relation in Eq. (7). Given the difficulty of obtaining reliable modulation wavelength over the various We numbers, we leave the detailed study of the We (in)dependence to future work. Instead, we focus our analysis on the proposed scaling $\sim \hat{t}R_0$ in the denominator. Figure 10 shows liquid tin sheets at $t \approx 0.33\tau_\mathrm{c}$ for initial droplet sizes of (a) 37, (b) 50, and (c) 70 µm, with We remaining approximately constant (ranging from 850 to 1200) providing discrete concentric modulations. (To keep the underlying plasma physics scale-invariant, we scale the laser pulse duration with the initial droplet radius, keeping the ratio of acceleration time to acoustic time constant[40].) Each panel presents averaged shadowgraphs composed of 20 frames, with the front view (left half) and back view (right half) displayed side by side. The averaging improves the signal-to-noise ratio and underscores the high reproducibility of the observed patterns. To qualitatively validate the inverse linear dependency on droplet radius, we perform left/right comparisons of front-view acquisitions for droplets with low Weber numbers but varying initial sizes. Specifically, for the case of a droplet with an initial diameter of 37 µm, the left-side front view is scaled by the ratio of the initial diameter relative to the diameter of the comparison sheet's droplet at a similar time. The results are shown in Fig. 10(d, e, f).

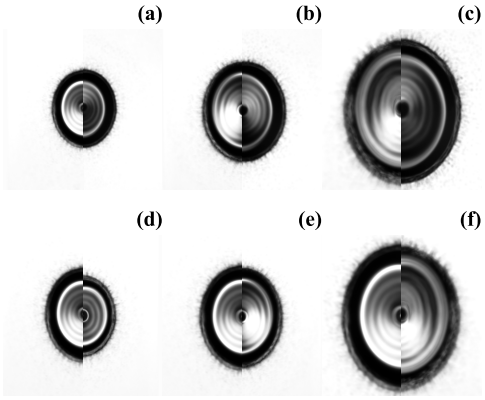

FIG. 10. Front (left) and back (right) views around $t/\tau_\mathrm{c} = 0.35$ of the following parameter sets [droplet diameter, laser pulse length, Weber number, and deformation Weber number] in (a) [37 µm, 10 ns, 1 200, 2 700], (b) [50 µm, 12 ns, 1 000, 2 700], (c) [70 µm, 20 ns, 850, 2 600]. Comparison of left side front views around $t/\tau_\mathrm{c} = 0.33$ of [37 µm, 1 200, 2 600] with mirrored (d) [45 µm, 10 ns, 700, 1 900 (e) [50 µm, 12 ns, 1 000, 2 700], (f) [70 µm, 20 ns, 850, 2 600].

For example, in Fig. 10(d), the left side of the 37 µm front view sheet is scaled by 45 µm/37 µm and compared with a mirrored left-side front view of a 45 µm droplet sheet. In this comparison, the sheets are not perfectly matched in

size, which is simply attributed to (minor) differences in the Weber deformation number We_d and therefore the kinetic energy of deformation. When We_d values are more similar, as in Fig. 10(e, f), the sheet radii align more closely, and after scaling, the modulation reflection pattern is very nearly identical, underlying the proposed scaling $1/R_0$ of Eq. (7).

So far, we have found agreement on the order of magnitude of the modulations' wavelength and amplitude in comparing our observations to the three-phase R-T model, particularly so given the strong simplifications in the model, and experimental complexities in accurately determining wavelength and amplitude. However, there are still some observations that are not straightforwardly explained by the current model of the R-T instability. Firstly, we observe modulations that are predominantly cylindrically symmetric, indicating a suppression of azimuthal modulations at intermediate We numbers. This suppression could be explained by considering the (integer) number of azimuthal waves that need to fit on any individual radial wave. This explanation is partially supported by the observation that the azimuthal modulations are first observed on the outer radii [cf. Fig. 2(c)] where the larger circumference allows azimuthal modes to fit. Secondly, we find that new (concentric) modulations appear from the center region (cf. Fig. 3). This could hint at a driving mechanism separate from the early-time R-T instability, from which the hypothesis could be derived that the concentric modulations have an origin separate from the azimuthal ones. However, when azimuthal modulations are observed, they have a wavelength that is similar (same order) to the local concentric ones [cf. Fig. 2(c)] – such an implied coincidence would rather point towards a common R-T origin. Thirdly, we observe again that the modulation wavelength depends on the radial coordinate. Such implied *local* stretching, roughly proportional to the radial coordinate, is not captured in the current model[28], as may be expected given the assumption of a simple flat-disk geometry and uniform stretch [Eq. (5)]. Also, along with the radial local stretching, any temporal stretching dynamics is not adequately captured by the model. Lastly, as noted in Sec. III A, varying the Weber numbers results in different modulation patterns, although no definitive scaling could be obtained given the aforementioned difficulties of extracting a modulation wavelength from the data. Any visible changes may well be caused not by differences in the radial modulation wavelength, but rather by changing visibility of azimuthal modulations.

V. CONCLUSIONS

We present concentric surface modulations observed in reflection from both sides of laser-propelled and expanding liquid tin sheets, for droplets ranging from 27 to 70 μm in diameter at intermediate Weber numbers between 1 000 and 7 000. Through combined optical inspection in reflection and transmission modes, we determine that these surface modulations are only of order $\sim$10 nm in amplitude, on sheets with an average thickness of several 100 nm. The modulations appear predominantly front-back mirror symmetric (out-of-phase), and are highly reproducible.

We interpret these modulations as a manifestation of the instabilities that drive sheet breakup, as described by Klein et al.[28]. This study provides a clear and direct observation of such modulations. Furthermore, it reveals a (relatively) low-We counterpart of highly modulated sheets prior to sheet breakup. It provides experimental evidence of low-amplitude surface modulations in free-flying liquid sheets. We find qualitative agreement, in terms of the order of magnitude of the modulations' amplitude and wavenumber, with a model[28] based on a Rayleigh-Taylor instability that links the instantaneous wavenumber k to the system parameters, showing that $k(t/\tau_c)R_0 \sim (\tau_c/t)$, a scaling that is independent of the Weber number. Several aspects however remain insufficiently explained by the model such as (i) the concentricity of the perturbations and suppression of azimuthal modulation at low We number; (ii) the appearance of new modulations with time; (iii) the overall dynamics of the modulations. Moreover, there is a clear We number dependence of the visibility of azimuthal modes that is not yet understood. All such aspects have been brought to the forefront by the current work that is aimed to be a stepping stone for next works, which may include numerical studies, towards understanding the instability modes on thin sheets as produced from laser impact, a topic of particular relevance for stable target shaping in EUV lithography.

ACKNOWLEDGEMENTS

This work was conducted at the Advanced Research Center for Nanolithography (ARCNL), a public-private partnership between the University of Amsterdam (UvA), Vrije Universiteit Amsterdam (VU), Rijksuniversiteit Groningen (UG), the Dutch Research Council (NWO), and the semiconductor equipment manufacturer ASML and was partly financed by 'Toeslag voor Topconsortia voor Kennis en Innovatie (TKI)' from the Dutch Ministry of Economic Affairs and Climate Policy. This publication is also a part of the project 'Plasma driven by a variable-wavelength laser for next-generation EUV sources for nanolithography' (with project number 19458) of the Open Technology Programme which is financed by NWO. We thank Hugo França, Randy Meijer, Arie den Boef, Dmitry Kurilovich, and Bo Liu for useful discussions and Laurens van Buuren for assistance on the setup.

DISCLOSURES

The authors have no conflicts to disclose.

DATA AVAILABILITY STATEMENT

Data underlying the results presented in this paper may be obtained from the authors upon reasonable request.

APPENDIX A

Table I provides further details of the experiments discussed in the main text.

D_0 [μm]	d [μm]	τ [ns]	E [mJ]	t/τ_c	We	We_d	Fig.
31	100	10	5	0.2	800	1 200	2(a)
			10	0.2	1 700	2 300	2(b)
							3 (a-d)
			15	0.24	3 100	4 200	1(g)
							6(a)
							7(a)
			15	0.38	3 100	4 200	1(h)
							6(b)
							7(b)
			25	0.2	4 700	5 800	2(c)
			50	0.2	12 000	10 600	2(d)
50	90	15	–	0.3	123 000	57 000	2(e,f)
		12	7.8	0.33	1000	2 700	10(b)
27	100	10	Δ	0.4	7 000	–	8(c)
36	100	10	–	0.31	1 400	3 900	6 (a,b)
37	90	10	7.4	0.35	1 200	2 700	10(a)
45	90	10	6.4	0.35	700	1 900	10(e)
70	95	20	10	0.35	850	2 600	10(c)

TABLE I. Details for shadowgraphs containing droplet diameter (D_0), beam spot size (d), pulse duration (τ), PP energy (E), non-dimensional time (t/τ_c), measured Weber number (We), measured Weber deformation number (We_d), and figure(panel) usage (Fig.).

APPENDIX B

Figure 11 provides further details of the experimental setup.

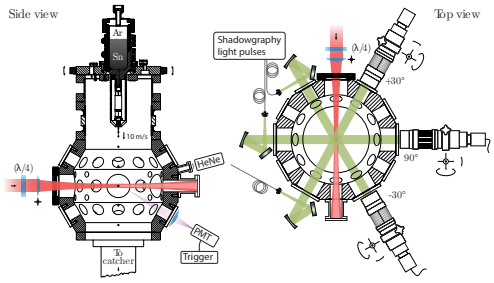

FIG. 11. Schematic of the experiment. Figure modified from Ref. 41.

[1]V. Bergeron, D. Bonn, J. Y. Martin, and L. Vovelle, Nature **405**, 772âĂŞ775 (2000).
[2]C. Josserand and S. Thoroddsen, Annu. Rev. Fluid Mech. **48**, 365âĂŞ391 (2016).
[3]B. L. Scheller and D. W. Bousfield, AIChE J. **41**, 1357âĂŞ1367 (1995).
[4]Y. Wang and L. Bourouiba, J. Fluid Mech. **814**, 510âĂŞ534 (2017).
[5]E. Villermaux and B. Bossa, J. Fluid Mech. **668**, 412âĂŞ435 (2011).
[6]A. Rozhkov, B. Prunet-Foch, and M. Vignes-Adler, Phys. Fluids **14**, 3485âĂŞ3501 (2002).
[7]X. é. Huang, X. è. Dong, J. æ. Li, and J. å. Liu, Phys. Fluids **31**, 062106 (2019).
[8]Y. Wang, R. Dandekar, N. Bustos, S. Poulain, and L. Bourouiba, Phys. Rev. Lett. **120**, 204503 (2018).
[9]S. Kooij, R. Sijs, M. M. Denn, E. Villermaux, and D. Bonn, Phys. Rev. X **8**, 031019 (2018).
[10]D. Lohse, Annu. Rev. Fluid Mech. **54**, 349âĂŞ382 (2022).
[11]B. Derby, Annu. Rev. Mater. Res. **40**, 395âĂŞ414 (2010).
[12]V. Bakshi, ed., *EUV Lithography*, 2nd ed. (SPIE Press) p. 758.
[13]O. O. Versolato, Plasma Sources Sci. Technol. **28**, 083001 (2019).
[14]H. Gelderblom, H. Lhuissier, A. Klein, W. Bouwhuis, D. Lohse, E. Villermaux, and J. Snoeijer, J. Fluid Mech. **794**, 676 (2016).
[15]H. Mizoguchi, T. Abe, Y. Watanabe, T. Ishihara, T. Ohta, T. Hori, A. Kurosu, H. Komori, K. Kakizaki, A. Sumitani, O. Wakabayashi, and H. Nakarai, Proc. SPIE **7636**, 763608 (2010).
[16]I. Fomenkov, D. Brandt, A. Ershov, A. Schafgans, Y. Tao, G. Vaschenko, S. Rokitski, M. Kats, M. Vargas, M. Purvis, R. Rafac, B. La Fontaine, S. De Dea, A. LaForge, J. Stewart, S. Chang, M. Graham, D. Riggs, T. Taylor, M. Abraham, and D. Brown, Adv. Opt. Technol. **6**, 173âĂŞ186 (2017).
[17]T. Sizyuk and A. Hassanein, Phys. Plasmas **27**, 103507 (2020).
[18]B. Liu, R. A. Meijer, W. Li, J. Hernandez-Rueda, H. Gelderblom, and O. O. Versolato, Phys. Rev. Appl. **20**, 014048 (2023).
[19]H. B. Squire, Br. J. Appl. Phys. **4**, 167 (1953).
[20]G. Taylor, Proc. R. Soc. Lond. A **259**, 1 (1961).
[21]E. Villermaux and C. Clanet, J. Fluid Mech. **462**, 341âĂŞ363 (2002).
[22]C. Clanet and E. Villermaux, J. Fluid Mech. **462**, 307âĂŞ340 (2002).
[23]R. Li and N. Ashgriz, Phy. Fluids **18**, 087104 (2006).
[24]N. Bremond and E. Villermaux, J. Fluid Mech. **524**, 121âĂŞ130 (2005).
[25]F. P. Buff, R. A. Lovett, and F. H. Stillinger, Phys. Rev. Lett. **15**, 621 (1965).
[26]O. Krichevsky and J. Stavans, Phys. Rev. Lett. **73**, 696 (1994).
[27]A. Vledouts, J. Quinard, N. Vandenberghe, and E. Villermaux, J. Fluid Mech. **788**, 246âĂŞ273 (2016).
[28]A. L. Klein, D. Kurilovich, H. Lhuissier, *et al.*, J. Fluid Mech. **893**, A7 (2020).
[29]B. Liu, R. A. Meijer, J. Hernandez-Rueda, D. Kurilovich, Z. Mazzotta, S. Witte, and O. O. Versolato, J. Appl. Phys. **129**, 053302 (2021).
[30]H. K. Schubert, D. J. Engels, R. A. Meijer, B. Liu, and O. O. Versolato, Phys. Rev. Res. **6**, 023182: 1 (2024).
[31]B. Liu, D. Kurilovich, H. Gelderblom, and O. O. Versolato, Phys. Rev. Appl. **13**, 024035 (2020).
[32]I. P.-O. Company, *Model K2 DistaMax OEM Handbook* (2021), retrieved from `https://www.infinity-usa.com/wp-content/uploads/Model-K2-DistaMax-OEM-Handbook-090121.pdf`.
[33]S. J. Byrnes, arXiv (2016).
[34]D. Kurilovich, M. M. Basko, D. A. Kim, F. Torretti, R. Schupp, J. C. Visschers, J. Scheers, R. Hoekstra, W. Ubachs, and O. O. Versolato, Phys. Plasmas **25**, 012709 (2018).
[35]B. Liu, J. Hernandez-Rueda, H. Gelderblom, and O. O. Versolato, Phys. Rev. Fluids **7**, 083601 (2022).
[36]J. Hernandez-Rueda, B. Liu, D. J. Hemminga, Y. Mostafa, R. A. Meijer, D. Kurilovich, M. Basko, H. Gelderblom, J. Sheil, and O. O. Versolato, Phys. Rev. Res. **4**, 013142 (2022).
[37]H. Xia, M. Shats, and H. Punzmann, Europhys. Lett. **91**, 14002 (2010).
[38]G. Cisneros, J. S. Helman, and C. N. J. Wagner, Phys. Rev. B **25**, 4248 (1982).
[39]S. A. Reijers, D. Kurilovich, F. Torretti, H. Gelderblom, and O. O. Versolato, J. Appl. Phys. **124**, 013102 (2018).
[40]R. A. Meijer, D. Kurilovich, K. S. E. Eikema, O. O. Versolato, and S. Witte, J. Appl. Phys. **131**, 105905 (2022).
[41]R. Meijer, *Tailored Laser-Droplet Interaction. For Target Formation in Extreme Ultraviolet Sources*, Ph.D. thesis, VU University Amsterdam (2021), published on 4 October 2021.